Article

Effect of Segregation and Surface Condition on Corrosion of Rheo-HPDC Al–Si Alloys

Maryam Eslami [1] [iD], Mostafa Payandeh [2], Flavio Deflorian [1], Anders E. W. Jarfors [2] [iD] and Caterina Zanella [2],* [iD]

[1] Department of Industrial Engineering, University of Trento, 38123 Trento, Italy; maryam.eslami@unitn.it (M.E.); flavio.deflorian@unitn.it (F.D.)

[2] Department of Materials and Manufacturing, School of Engineering, Jönköping University, 55111 Jönköping, Sweden; mostafa.payandeh@ju.se (M.P.); anders.jarfors@ju.se (A.E.W.J.)

* Correspondence: caterina.zanella@ju.se; Tel.: +46-36-10-1691

check for updates

Abstract: Corrosion properties of two Al–Si alloys processed by Rheo-high pressure die cast (HPDC) method were examined using polarization and electrochemical impedance spectroscopy (EIS) techniques on as-cast and ground surfaces. The effects of the silicon content, transverse and longitudinal macrosegregation on the corrosion resistance of the alloys were determined. Microstructural studies revealed that samples from different positions contain different fractions of solid and liquid parts of the initial slurry. Electrochemical behavior of as-cast, ground surface, and bulk material was shown to be different due to the presence of a segregated skin layer and surface quality.

Keywords: Al–Si alloys; rheocasting; HPDC; electrochemical evaluation

1. Introduction

High pressure die casting (HPDC) is one of the most used manufacturing process for light alloy components [1,2], due to its high productivity, capability to cast complex geometry, dimensional accuracy, reduced need for finishing operations, and producing component with fine grain microstructure and good mechanical properties [3–5].

Coupling semisolid metal (SSM) casting to HPDC (SSM-HPDC) is a promising technology to produce high quality components with sound microstructure. Higher viscosity of semisolid material in this process reduces air entrapment and consequent porosity in the component. Such a technology introduces a new opportunity to enhance the castability of a component, which is impossible to achieve by traditional manufacturing methods [2,3,6,7].

There are two kinds of semisolid processes: "rheocasting" and "thixocasting". In 1976, Flemings et al. [8] introduced rheocasting as an alternative manufacturing process to die casting and even forging, and suggested it can be used to prepare high quality parts. Rheocasting, the method which is used in the current research, involves shearing force during a first solidification to produce a slurry. The slurry is then transferred into a mold and solidifies with non-dendritic microstructure [9]. Rheocasting can be coupled with high pressure die casting and Rheo-HPDC parts have a globular microstructure and usually show low porosity. This leads to heat treatability and high performance [2,6]. Proper materials for Rheo-HPDC process are limited to those which have good castability with HPDC process and also have low sensitivity of the solid fraction to variations of temperature [10]. Hypoeutectic Al–Si alloys in the range of 5–8% silicon content are suitable choices for this process [11].

While Rheo-HPDC widens the composition range of castable alloys and allows for casting of thin sections, it is a process which increases the inhomogeneity of the microstructure at the macroscale in the final component, in comparison to the conversional HPDC process [5]. This phenomenon arises from the fact that the primary α-Al phase solidifies at higher temperature during slurry preparation, and is characterized with low solubility of alloying elements, therefore, these elements will be higher in the remnant liquid phase [11]. In addition, macrosegregation is formed during the filling process: solid and liquid fractions tend to separate in the gating system (longitudinal macrosegregation) and from the surface to the core of the component (transverse macrosegregation), increasing the microstructure inhomogeneity of the final component. This leads to variations of properties in different locations of the component either in microscopic or macroscopic scale [12–14]. The liquid will preferentially fill the furthest parts of the mold, or the thinner sections, while the solid fraction will concentrate in the core. This is due to the higher viscosity of the slurry compared to the liquid molten metal during casting [15]. As a consequence, higher yield strength and ultimate tensile strength are developed near the vent, where more liquid fraction and refined grains solidify compared to the region near the gate [11].

Park et al. [16] showed that the tensile elongation of thixoformed 357-T5 semi solid aluminum alloy is strongly affected by the α_1-Al volume fraction which changes in different locations of the component.

Masuku et al. [17–19] investigated the corrosion behavior of the surface layer of SSM-HPDC 7075-T6 and 2024-T6 alloys in sodium chloride solution. They observed a surface liquid segregated layer (mainly formed by the eutectic) in all the alloys, with higher amounts of alloying elements (such as copper). They did not report any difference between the pitting potential, however, they mentioned that pitting morphology is affected by the amount and distribution of the intermetallic particles and therefore differences are expected between the SSM-HPDC and wrought alloys [18]. How longitudinal macrosegregation affects the corrosion resistance of semisolid aluminum alloys and the behavior of the as-cast surface is still not studied.

Limitation of scientific and technical knowledge makes it essential to evaluate properties and behavior of aluminum alloys produced by means of Rheo-HPDC process under different operational circumstances. Corrosion resistance is a critical property for Al alloys, especially in outdoor applications, and therefore, is an interesting subject either for researchers or industries.

Many authors have investigated corrosion resistance of Al–Mg–Si (6xxx series) [20–28] and Al–Si alloys [29–35]. Regarding Al–Mg–Si alloys, pitting and intergranular corrosions (IGC) have been reported as localized corrosion features [23,27]. IGC susceptibility is especially influenced by the amount of copper, iron, and Mg/Si ratio in the alloy composition [23,24,27,36,37]. The localized corrosion occurs in the presence of phases such as β-phase (Mg_2Si), silicon (in alloys with excess Si) and copper-containing phases such as Q-phase ($Al_4Cu_2Mg_8Si_7$) (in alloys with Cu) [38]. Iron-rich intermetallics in Al–Mg–Si alloys are nobler compared to the matrix [21]. Nobler intermetallic particles (IMs) in grain boundaries form a microgalvanic couple with the adjacent precipitate free zones (PFZ), and result in IGC [37]. In chloride containing solutions, Mg_2Si undergoes Mg dealloying, before turning to an active cathodic site [21,22].

Al–Si alloys generally suffer from the localized corrosion (pitting) in the Al–Si eutectic, due to impurities, such as Fe [39]. Generally, corrosion behavior of these alloys depends on the amount and morphology of iron-rich IMs, such as β-AlFeSi and π-AlFeSiMg [34]. Both Fe and Si are cathodic with respect to the aluminum. Therefore, together they can form a microgalvanic couple, resulting in localized corrosion [34]. Silicon also increases the corrosion potential [23,27].

Previous corrosion studies of semisolid-cast Al-Si alloys such as those performed by Yu et al. [40], Park et al. [31], Tahamtan et al. [30,35] and Arrabal et al. [34], have mostly emphasized on the pitting corrosion in the eutectic regions of A356 and A357 alloys.

It is shown that semisolid-cast process, such as thixoforming, can effectively modify the Si morphology in 357 alloy, resulting in a higher corrosion resistance [40]. The acicular eutectic silicon phase in permanent mold cast 357 alloy has more contact area with the aluminum matrix in comparison

to that of the globular eutectic silicon in the thixoformed alloy, and this can encourage the galvanic corrosion [40].

Rheocast process can increase the concentration of silicon in α-Al particles in A356 aluminum alloy. This leads to smaller potential differences between this phase and the eutectic silicon phase and β-AlFeSi IM particles, which result in higher resistance to pitting corrosion [34]. Although both of the eutectic silicon phase and iron-rich IMs contribute in the localized corrosion, some authors consider the contribution of IM particles to be more important [34,41].

The present study focused on the Al low Si alloys produced by Rheo-HPDC process and on the effect of the microstructure inhomogeneity on the corrosion resistance. In addition, the influence of silicon content and surface condition on the microstructure characteristics and the corrosion behavior is examined.

2. Materials and Methods

A telecom cavity filter (Figure 1) was rheocast by a 400 ton HPDC machine equipped with an automated RheoMetal™ slurry generator. The RheoMetal™ (Stockholm, Sweden) process uses an Enthalpy Exchange Material (EEM) as slurry generator [42].
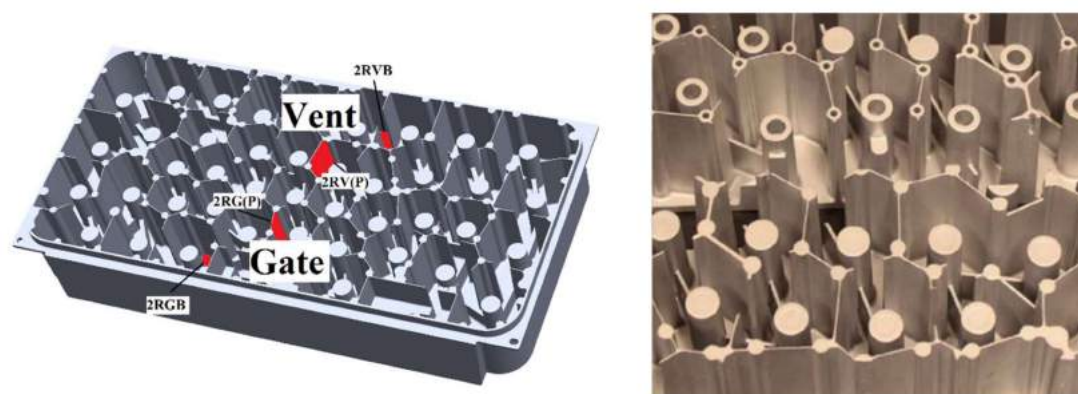
Figure 1. The experimental cavity filter used for Rheo-high pressure die cast (HPDC) process.

The alloys were prepared, and their composition were adjusted by adding pure silicon to a primary alloy in a resistance furnace. The chemical compositions of the alloys were measured by optical emission spectroscopy (OES) (SPECTRO Analytical Instruments GmbH, Kleve, Germany) and are presented in Table 1.

Table 1. Measured composition (wt %) of alloys.

Name	Si	Fe	Cu	Mn	Mg	Zn	Al
Alloy 2.5	2.41	0.462	0.131	0.019	0.58	0.038	96.338
Alloy 4.5	4.50	0.481	0.137	0.019	0.58	0.035	94.223

In the casting process, the temperature of the fixed half of the die was maintained at 230–250 °C, while the temperature of the moving half was set to 280–320 °C. Shots of about 5 kg were held at 675 °C in the ladle where 5% of EEM was added under stirring at 900 rpm. The final slurry temperature was 610 °C and had 40% of solid fraction. The die was filled in two stages with piston speed at 0.23 and 5.2 m/s, respectively, and the shot time was 31 ms. The solid fraction in the slurry was estimated by image analyses of a quenched sample of slurry after light etch using a 5% NaOH.

Specimens for corrosion tests were taken from the thin walls (thickness ≈ 1.5 mm), in as-cast or ground condition, or from the thick bottom plate (thickness ≈ 4 mm), underneath the component only in ground condition.

To investigate longitudinal segregation, both thin wall and thick bottom plate samples were taken from different locations: near the feeding gate (G) or near the die vent (V). The detailed samples designation is presented in Table 2.

Table 2. Designation of samples.

Name	Section	Near the Gate	Near the Vent
Alloy 2.5	Thin wall surfaces	2.5 RGP	2.5 RVP
	Plate bulk	2.5 RGB	2.5 RVB
Alloy 4.5	Thin wall surface	4.5 RGP	4.5 RVP
	Plate bulk	4.5 RGB	4.5 RVB

R = Rheo-HPDC, G = Samples from near the gate, V = Samples from near the vent, P = Thin wall samples in ground surface condition, B = Samples from the thick bottom plate ground to the half of thickness (Bulk samples).

Polarization tests and electrochemical impedance spectroscopy (EIS) were performed with a 3-electrode cell and a potentiostat (Parstat 2273, Ametek, Berwyn, PA, USA). The aluminum alloy with an exposure area of 1 cm^2 was connected as working electrode, platinum as a counter and silver/silver chloride (Ag/AgCl·3M·KCl) as reference electrodes. Due to the working environment of telecom components, diluted Harrison solution (0.5 g/L NaCl and 3.5 g/L $(NH_4)_2SO_4$) was used to simulate the electrochemical behavior of the alloys exposed to an acid rain [43,44].

Regarding the polarization test, the sweep rate was 0.166 mV/s, and the delay time before each the test was 600 s, to let the open circuit potential (OCP) reaches its stable value. For each sample, mainly anodic branch was collected (as cathodic branch did not exhibit any significant information), starting from OCP. Anodic polarization was stopped after the maximum current density of 9×10^{-4} A/cm^2 was reached. In order to highlight the effect of chloride ions, all the polarization experiments were also repeated using a solution of 3.5 g/L $(NH_4)_2SO_4$.

EIS measurements were collected for 24 h of immersion at the room temperature in the diluted Harrison solution from 100 kHz to 10 MHz with 36 points and 10 mV of amplitude of the sinusoidal potential.

EIS measurements were conducted on as-cast and ground surfaces of thin wall samples, and also on ground surface of the thick bottom plate samples, to investigate the effect of transverse macrosegregation and as-cast condition.

To distinguish the results of these different experiments, the letter P is added to the name of the samples of thin walls, which were ground before the electrochemical test. These samples were wet ground by silicon carbide abrasive papers from P600 to P4000 to the extent that the skin layer was completely removed. In the case of bulk samples (of the thick bottom plate), the surfaces were ground until the middle of each sample was reached. In this way, the electrochemical behavior of the bulk of each alloy can be investigated. Repeatability of the results was tested by conducting each experiment on at least three specimens. ZsimpWin^{TM} software (3.5, Echem software, Ann Arbor, MI, USA, 2013) was used to fit the EIS spectra. After the corrosion tests, corroded surfaces were examined using SEM/EDS (JSM-IT300) (Jeol, Akishima, Japan).

For metallographic analyses, samples were wet ground, followed by polishing using diamond paste (3 μm and 1 μm). NaOH solution (10 wt %) was used to clean the surface and to reveal the constituents of the microstructure. The microstructure of the surfaces and the bulk of components were studied using a light optical microscope (LOM) (Zeiss, Oberkochen, Germany) and scanning electron microscopy (SEM) (Jeol, Akishima, Japan). Energy/wave-dispersive X-ray spectroscopy (EDS/WDS) (EDAX, Mahwah, NJ, USA) was used to measure the composition of the different phases.

3. Results and Discussion

3.1. Microstructural Features

Generally, the microstructure of rheocast low silicon content aluminum alloys exhibit the presence of α-Al phase together with Al–Si eutectic mixture and some intermetallic particles [45]. Based on the presence of Fe in the two alloys (Table 1), and since its solubility in Al is very low [46], the presence of Fe-rich intermetallic particles is expected. The sequence of phase formation (aluminum phase and eutectic reaction) was calculated using ThermoCalc[TM] (2015b, Solna, Sweden, 2015) software [47,48]. The results are shown in Figure 2. As it is predicted by the thermodynamic model, the needle shape β-AlFeSi intermetallic particle was the most favored intermetallic phase for precipitation, and it is formed before the eutectic silicon.
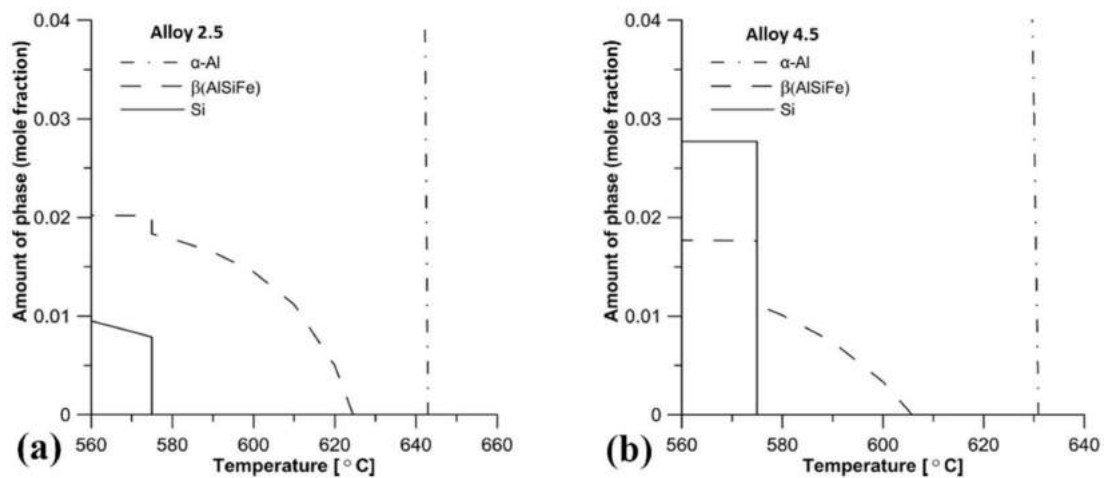

Figure 2. Sequence of formation of different phases in the (**a**) Alloy 2.5 and (**b**) Alloy 4.5.

The microstructural features of the polished surfaces of thin walls from different positions in the cavity, with different percentage of silicon, are illustrated in LOM images in Figure 3. From microstructure images in Figure 3, two different range sizes of α-Al phase can be observed: a coarse globular α-Al phase (α_1-Al) and a finer α-Al phase (α_2-Al).

The formation of α_1-Al and α_2-Al is related to the multi-stage solidification in the semisolid metal process. α_1-Al grains are nucleated in the ladle, under shear forces, due to stirring at a higher temperature due to contact with the EEM and form the slurry, while α_2-Al grains are mostly formed in the solidification stage inside the die, at a higher cooling rate [49].

Regarding the effect of the position, the microstructure near the gate (Figure 3a,c) consists of a higher amount of α_1-Al particles compared to the region near to the vent (Figure 3b,d). However, this difference is not significant in alloy 2.5.

This microstructure heterogeneity is attributed to the distribution among the die of the liquid and solid fraction of the slurry during the injection stage: the liquid part squeezes out and leaves the solid fraction behind near to the gate. Easton et al. [50] show this behavior in a SSM-HPDC component and defined this type of separation of the slurry as sponge effect.

α_2-Al particles in thin wall samples (of both alloys) are finer near the vent in comparison to the region near the gate, due to the higher undercooling in this region of the cavity. This effect is more evident for alloy 4.5. It seems that by increasing the amount of silicon, aluminum phase is refined by undercooling, which can be due to more nucleation of the eutectic silicon [51].
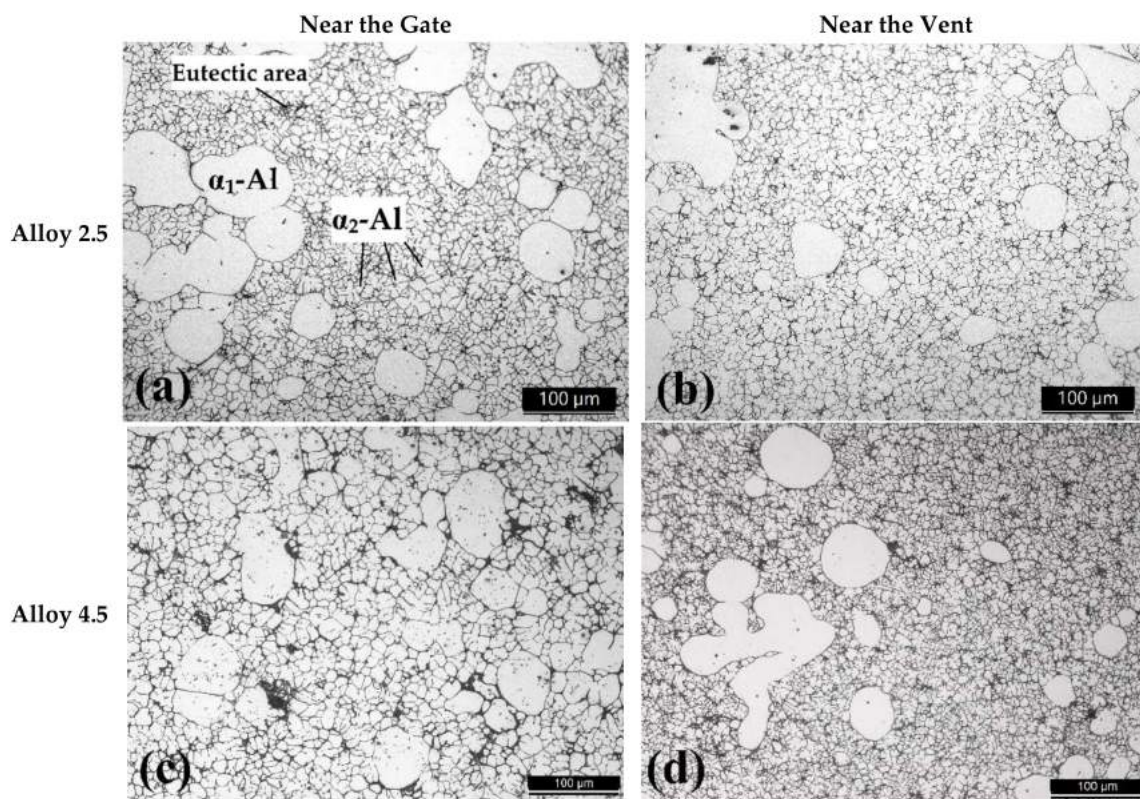
Figure 3. Light optical microscope (LOM) images of sample (**a**) 2.5 RGP; (**b**) 2.5 RVP; (**c**) 4.5 RGP and (**d**) 4.5 RVP.
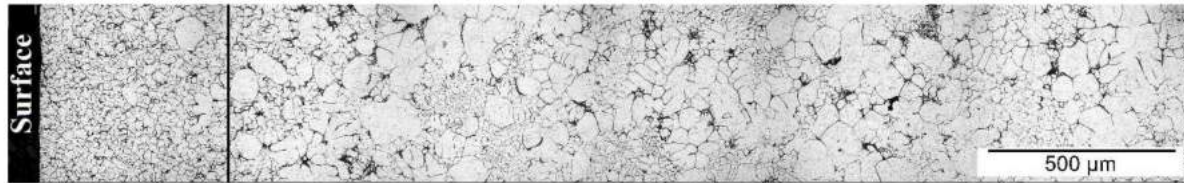
LOM images of sample 2.5 RGB and 4.5 RGB from the thick plate are presented in Figure 4. In comparison to the microstructure of thin walls, the bulk microstructure contains more α_1-Al particles in both of the alloys, which is expected. In fact, due to the high viscosity of semisolid slurry, thin walls are mostly filled by liquid, while the relatively thicker parts are filled by the solid fraction of the slurry [15].
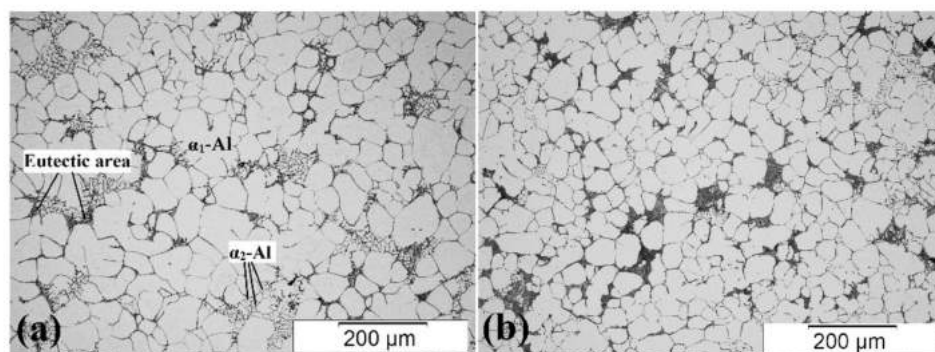
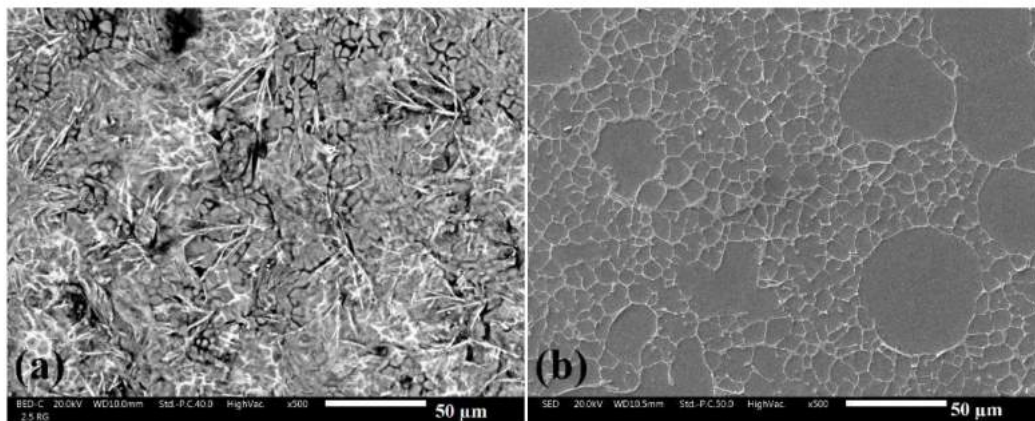**Figure 4.** LOM image of sample (**a**) 2.5 RGB and (**b**) 4.5 RGB.

LOM image of cross-section of the thick plate of Alloy 2.5 in the region near the gate is reported in Figure 5. On the surface, there is a segregation of the liquid fraction to the surface and α_1-Al solid fraction, which tend to aggregate in the center of samples. This phenomenon is considered as transverse macrosegregation. Three different phenomena lead to transverse macrosegregation: skin effect [12], sponge effect [13,50] and shearing band during melt flow that lead to porosity or

eutectic-rich segregation band [52]. Study of transverse macrosegregation in different positions of the same Rheo-HPDC component performed by Payandeh et al. [53] showed that the thickness of the surface segregation layer increases by increasing the liquid faction. Govender et al. [54] also reported the existence of a surface layer consisting of mainly liquid or eutectic phase in SSM-HPDC A356 Alloy.


Figure 5. LOM images of cross-sectional view of sample 2.5 RGB.

Figure 6 compares the as-cast and polished surfaces of sample 2.5RG/P of the thin wall section. It is noticeable how the as-cast surface is enriched with eutectic phase and intermetallic particles. Moreover, localized defects, such as porosities and/or voids among the grains and inclusions, are visible.

Figure 6. Scanning electron microscopy (SEM) image of sample (**a**) 2.5 RG (as-cast condition) and (**b**) 2.5 RGP (polished surface).

SEM image of sample 4.5 RGP at higher magnification in Figure 7a depicts the microstructure of the eutectic and the intermetallic particles. The Si particles have a flake shape and form a continuous network [55].
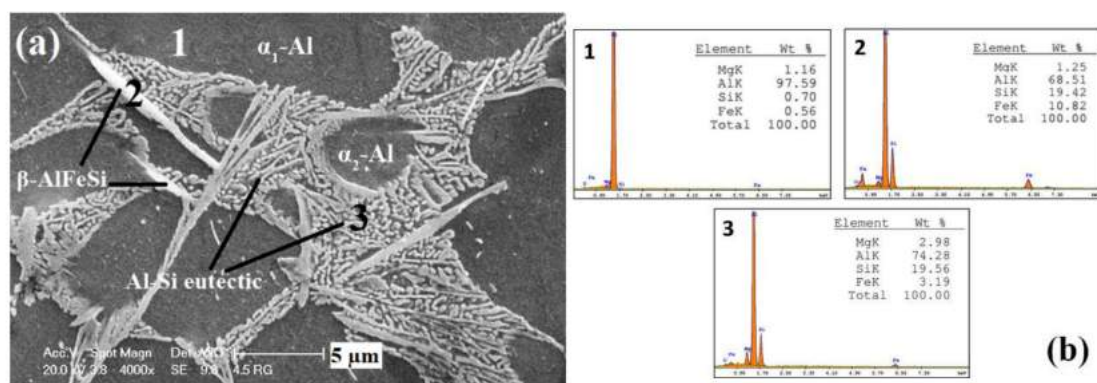
Figure 7. SEM image (**a**) and spot EDS analysis (**b**) of polished surface microstructure of the sample 4.5 RGP.

According to the EDS results in Figure 7b, in this figure, intermetallic particles are rich in iron, and as is expected in hypoeutectic alloys, the intermetallic particles are β-AlFeSi. These intermetallic particles usually have a needle shape [34], and a platelet morphology in 3D tomographic volume [56].

Figure 8 represents the concentration of silicon at the center of α_1-Al and α_2-Al grains in alloys 2.5 and 4.5. α_2-Al particles, nucleated from the liquid portion of the slurry [57], have higher amounts of silicon, which leads to smaller potential differences between them and the silicon eutectic phase and/or iron-rich intermetallic particles, and results in less severe corrosion [34].
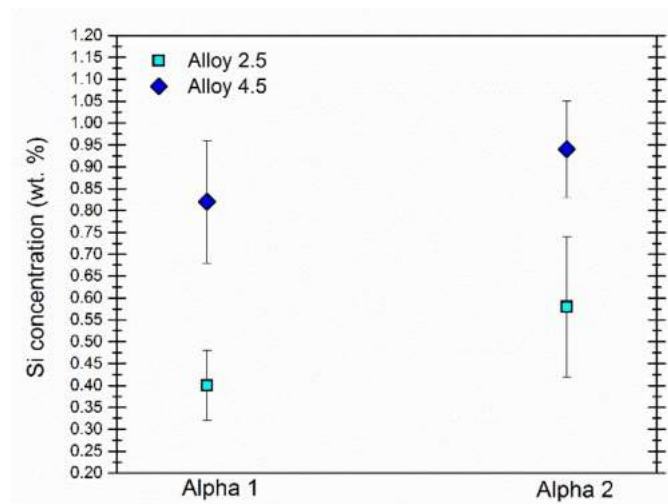

Figure 8. Concentration of Si in α_1 and α_2-Al phases in alloy 2.5 and 4.5.

3.2. Corrosion Studies

3.2.1. Potentiodynamic Polarization Curves

Potentiodynamic polarization curves of as-cast surface of the thin wall samples (2.5 RG, 2.5 RV, 4.5 RG, and 4.5 RV) in the diluted Harrison solution and in the solution of 3.5 g/L $(NH_4)_2SO_4$ are reported in Figure 9.

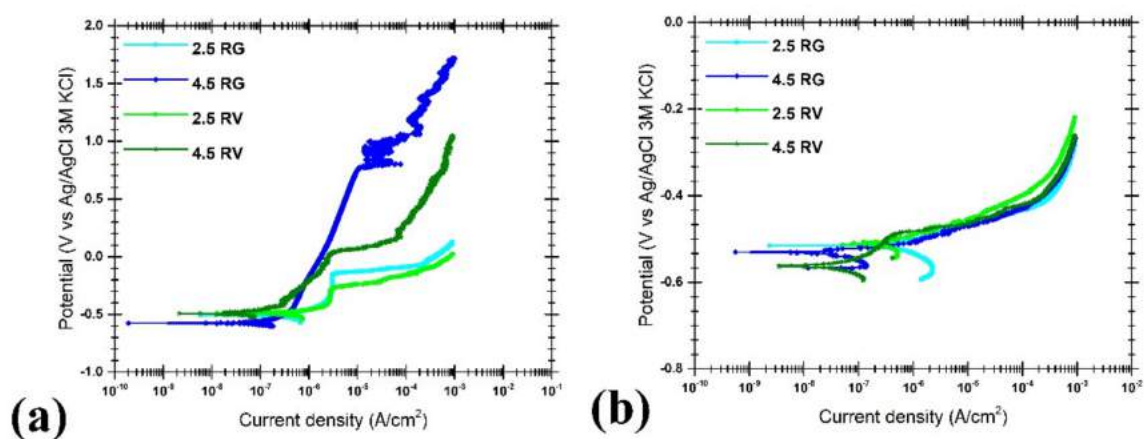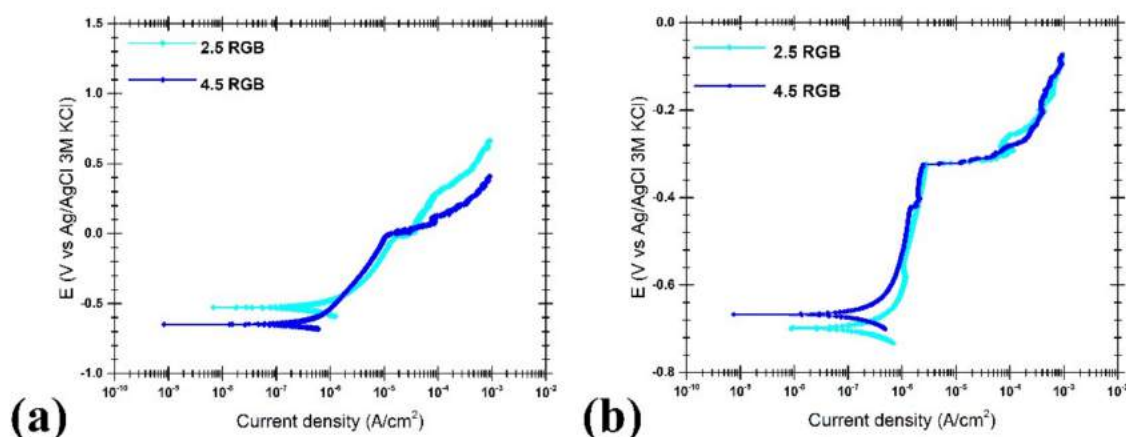**Figure 9.** Potentiodynamic polarization curves in (**a**) the solution of 3.5 g/L $(NH_4)_2SO_4$ and (**b**) the diluted Harrison solution.

In both of the solutions, values of corrosion potential are similar for different samples regardless of the position and the silicon content. Regarding the effect of the position, samples from near the gate

(2.5 RG and 4.5 RG) possess higher pitting potentials, in the solution of 3.5 g/L $(NH_4)_2SO_4$, compared to the samples taken from near the vent (2.5 RV and 4.5 RV). In the diluted Harrison solution, all of the samples (except for 4.5 RV) show pitting from the OCP, which is due to the chloride ions and the higher amount of iron-rich intermetallic particles, as well as the defective condition of the as-cast surfaces.

Considering the bulk microstructure, the results of potentiodynamic polarization test in the diluted Harrison solution and in the solution of 3.5 g/L $(NH_4)_2SO_4$, of samples of 2.5 RGB and 4.5 RGB, are presented in Figure 10. In both of the solutions, the corrosion potentials of the two samples shows no significant difference.

Figure 10. Potentiodynamic polarization curves in (**a**) the solution of 3.5 g/L $(NH_4)_2SO_4$ and (**b**) the diluted Harrison solution.

The stability of the passive oxide layer is higher for the bulk samples compared to the as-cast surface, especially in the chloride containing solution. This is due to the surface condition, since the bulk samples have higher α_1-Al fraction, less eutectic fraction, and are ground while the thin wall samples are tested in as-cast condition.

SEM images of the corroded surfaces of samples 2.5 RG and 4.5 RG after the polarization test in the diluted Harrison solution are presented in Figure 11. For both samples, corrosion is localized, and a galvanic couple between the eutectic silicon phase and/or iron-rich intermetallic particles and aluminum matrix can be observed.
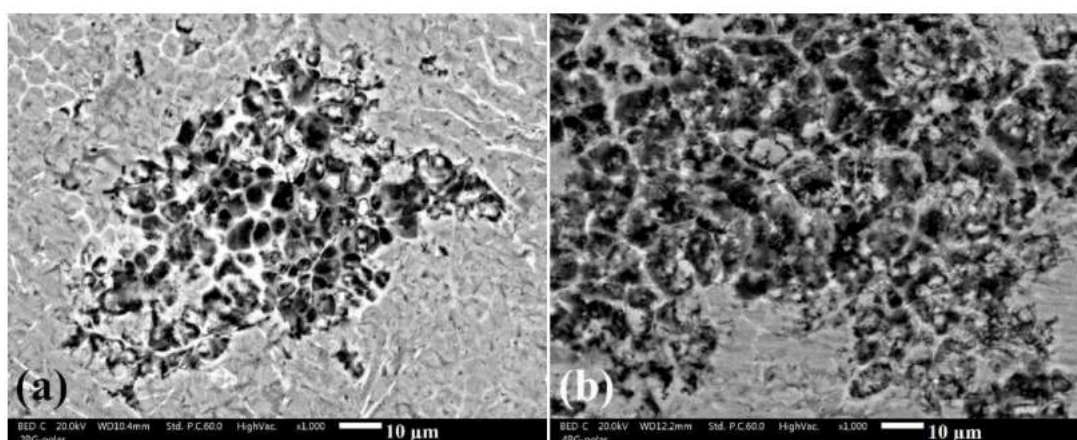
Figure 11. Corroded surfaces of sample (**a**) 2.5 RG and (**b**) 4.5 RG after polarization test in the diluted Harrison solution.

3.2.2. Electrochemical Impedance Spectroscopy

EIS spectra were obtained during 24 h of immersion in the diluted Harrison solution. The Bode plots of EIS spectra of thin wall samples in as-cast condition are reported in Figure 12. The figure also compares the effect of different positions in the cavity and the silicon content in the alloy.
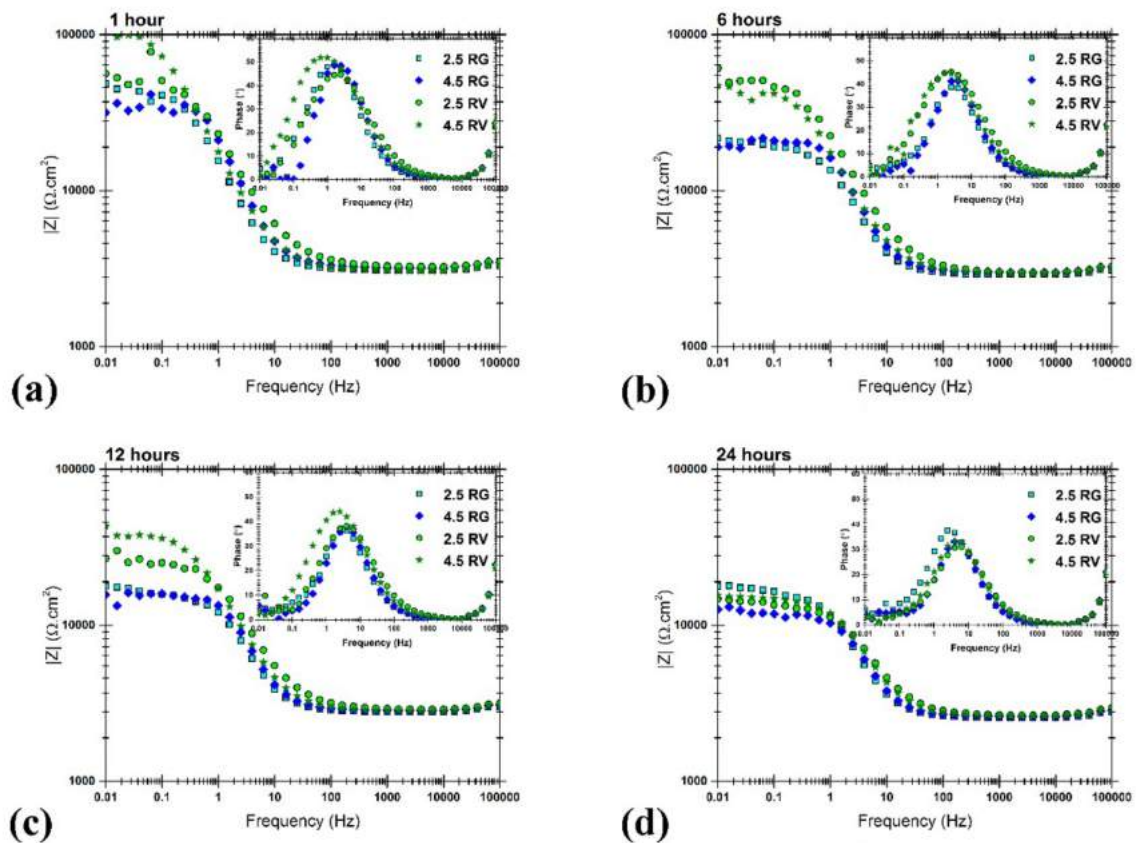
Figure 12. Bode plots of EIS spectra of samples 2.5 RG, 4.5 RG, 2.5 RV, and 4.5 RV after (**a**) 1 h; (**b**) 6 h; (**c**) 12 h; and (**d**) 24 h of immersion in the diluted Harrison solution.

For all of the samples, the impedance values at low frequencies decrease with the immersion time, which indicates the progressive corrosion process on the surface. In addition, the phase angle peak depresses through the immersion time, suggesting that the pitting corrosion activity is increasing [58].

Regarding the effect of position, samples taken from near the vent almost always, during the 24 h of immersion, show slightly higher impedance values at low frequencies, compared to the samples taken near the gate, except for 24 h, when all the samples show the same values. As it was discussed before, according to LOM images (Figure 3), the samples, which are taken from near the vent, possess a higher fraction of α_2-Al particles, and they also have a finer microstructure compared to the samples which are taken from near the gate.

Concerning the effect of silicon, no noticeable difference is detectable. However, all the previous research has indicated the positive effect of silicon on the pitting resistance of aluminum alloys [29,59,60]. Nevertheless, it is worth mentioning that these studies are focused on silicon content higher than 6%, which is higher than the percentage of silicon in both of our alloys.

To remove the effect of as-cast surface quality, the thin wall samples were ground using SiC abrasive papers to the extent that the skin layer was totally removed. The samples were then monitored by EIS during 24 h of immersion in the same solution. Bode presentation of EIS spectra of these samples are presented in Figure 13. According to these spectra, the ground thin wall samples show one order

of magnitude higher impedance values at low frequencies compared to the same samples in as-cast condition. In addition, the impendence values increased during 24 h of immersion for all of these samples. This can be related to the presence of a protective oxide, which is more stable to pitting. This protective oxide later is provided by better finishing quality on the ground surfaces. By grinding, the skin layer is removed, and a surface containing more α_1-Al particles and fewer intermetallic particles (Figure 6) is exposed to the corrosive solution.
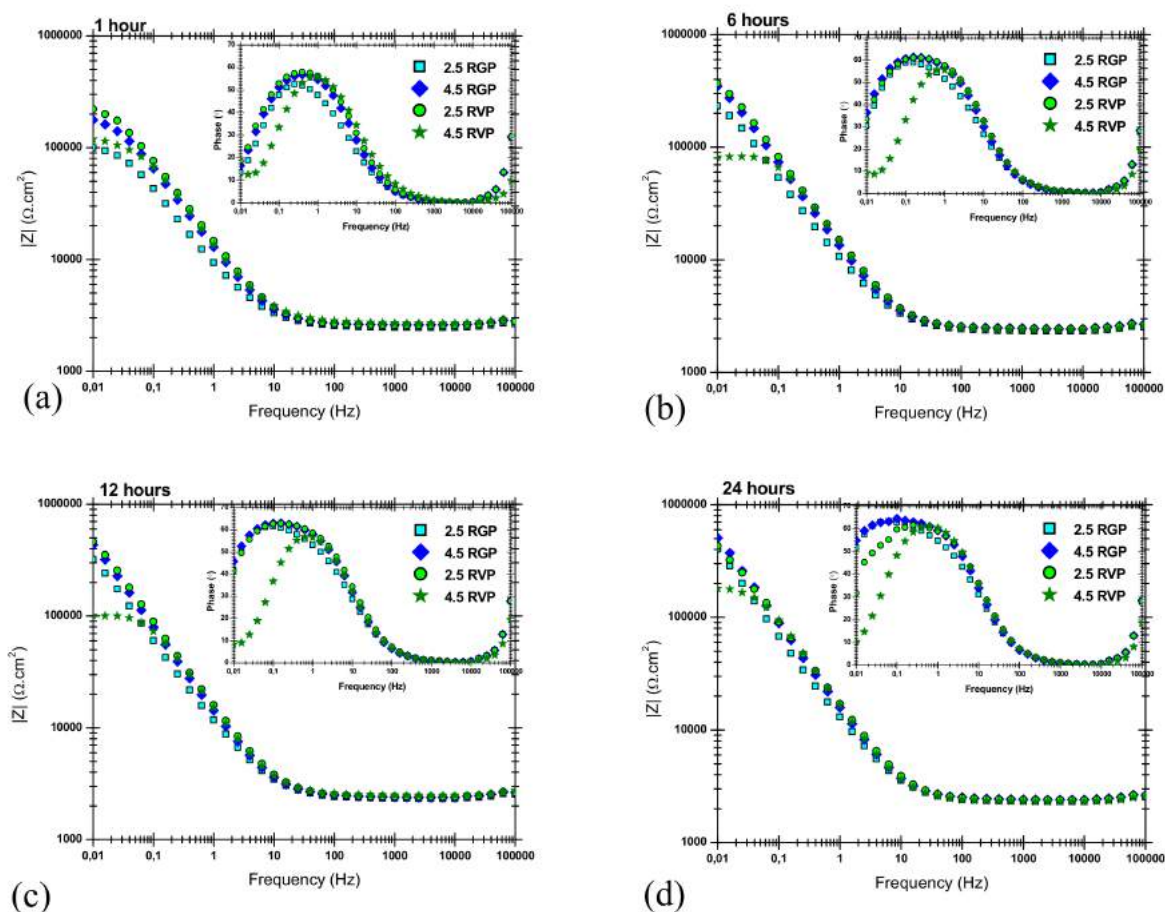
Figure 13. Bode plots of EIS spectra of samples 2.5 RGP, 4.5 RGP, 2.5 RVP, and 4.5 RVP after (**a**) 1 h; (**b**) 6 h; (**c**) 12 h and (**d**) 24 h of immersion in the diluted Harrison solution.

The difference between the corrosion performances of samples from different positions is negligible in this condition. Impedance tends slightly to increase after 6 h, and no pits are developed after 24 h. This proves that the poor behavior of as-cast surface is due to the poor surface quality and the higher amounts of intermetallic particles.

EIS spectra of the samples taken from the thicker plate, which are ground to the middle to expose the bulk microstructure, are reported in Figure 14. These results indicate the growth of a protective oxide layer on the surface.

The equivalent circuits used to describe the electrochemical responses of the samples 2.5 RG(P/B), 4.5 RG(P/B), 2.5 RVP, and 4.5 RVP are shown in Figure 15.

The electrochemical behavior of aluminum surface is affected by the presence of the passive oxide layer and the interface between the intermetallic particles and the aluminum. Although all these constituents are present, their time constants strongly overlap, or one dominates. Therefore, only one peak in the phase diagram can be observed for all of them.
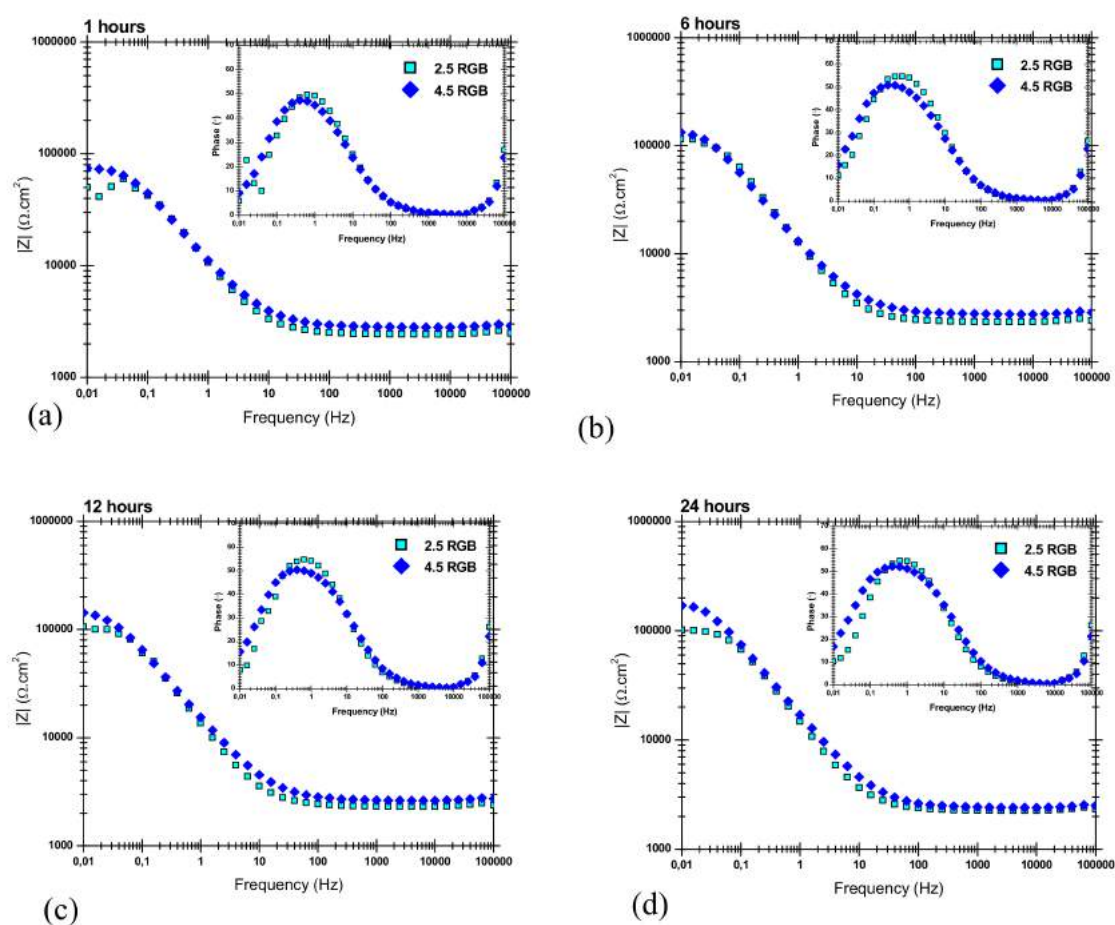
Figure 14. Bode plots of EIS spectra of samples 2.5 RGB, 4.5 RGB after (**a**) 1 h; (**b**) 6 h; (**c**) 12 h; and (**d**) 24 h of immersion in the diluted Harrison solution.
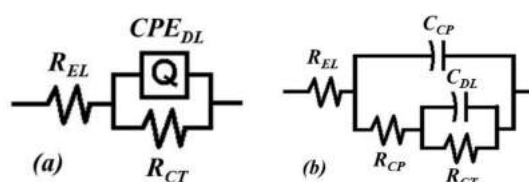
Figure 15. Equivalent circuits for the studied alloy after (**a**) a short time and (**b**) a longer time of immersion in the diluted Harrison solution.

The oxide layer is represented by a parallel circuit containing a resistor and a capacitor representing, respectively, the oxide ionic conduction and its dielectric properties [61].

The circuit in Figure 15a with one time constant has been used for the first 6 h of immersion, for almost all the samples, while the circuit in Figure 15b has been used for the later hours of immersion, when a second time constant was visible in the EIS spectrum. In the circuits depicted in Figure 15a,b, R_{EL} represents the resistance of the electrolyte. Q_{DL} (or C_{DL}) and R_{CT} stand for capacitive behavior of the electrical double layer at the interface between the surface and the solution, and for the resistance against the charge transfer (or polarization resistance), respectively. The second time constant at longer immersion time shows the oxidation of aluminum, and can represent the oxide layer (for ground surface of thin wall and thick plate samples). It can also stand for the corrosion products formed due to the localized corrosion attack in the case of thin wall samples in as-cast condition. R_{CP} and C_{CP} stand for the resistance and capacitive behavior of the oxide layer (or the corrosion products).

The fitting results of the two resistances (R_{CT} and R_{CP}) for thin wall samples, ground and in as-cast condition, and ground thick plate samples, are presented in Figures 16–18, respectively.
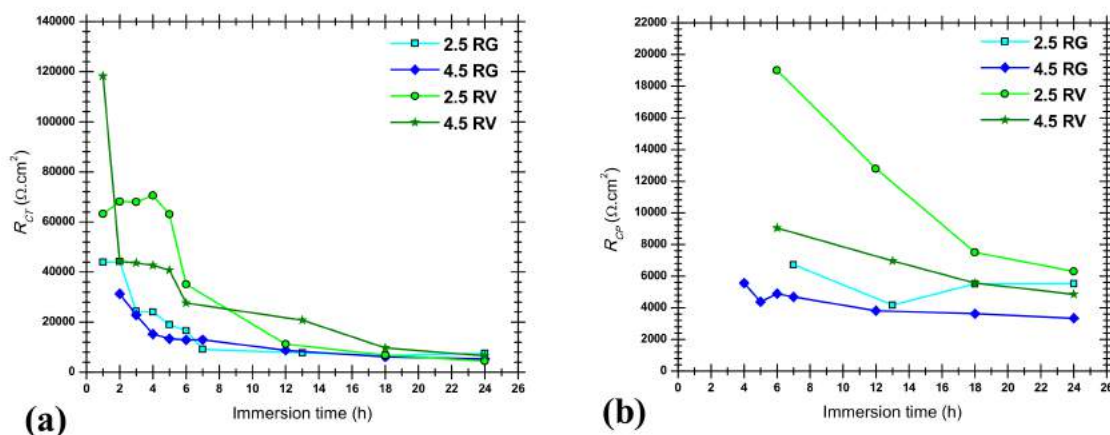

Figure 16. Fitted EIS parameters of as-cast thin wall samples: (**a**) R_{CT} and (**b**) R_{CP}.

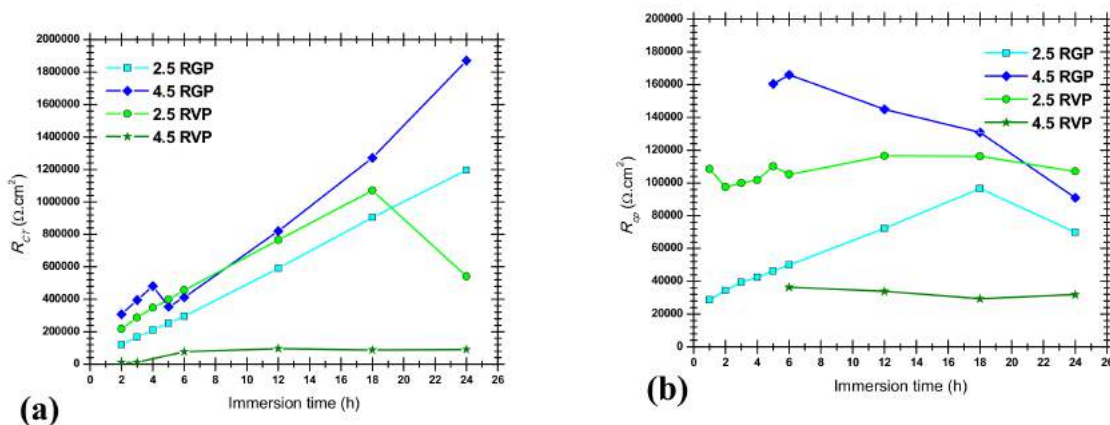**Figure 17.** Fitted EIS parameters of ground thin wall samples: (**a**) R_{CT} and (**b**) R_{CP}.
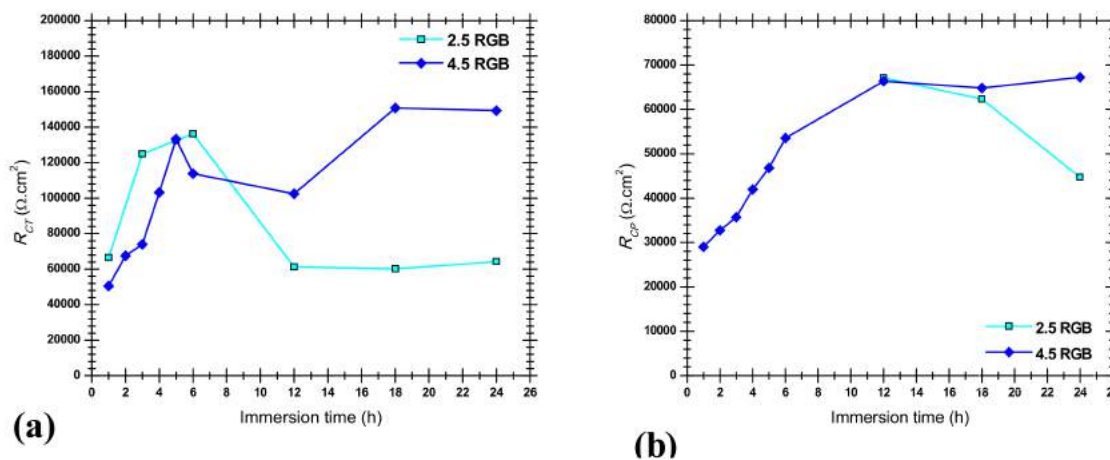

Figure 18. Fitted EIS parameters of ground thick plate (bulk) samples: (**a**) R_{CT} and (**b**) R_{CP}.

Values of R_{CT} of thin wall samples in as-cast condition (Figure 16a) decrease with the immersion time for all the samples, which indicates an increase of the activity and a higher corrosion rate in the

localized attack [62]. It should be noted that this decrease is immediate for the samples taken from near the gate, while for the samples taken from near the vent, it starts after 5–6 h of immersion. These values are higher for the samples near the vent, compared to the samples near the gate. Regarding the effect of silicon content, samples with lower amounts of silicon show slightly higher R_{CT} values at the very first hours of immersion. The values of R_{CP} (Figure 16b), that for these samples represent the resistance of corrosion products in the pits, are very low, and slightly decrease for all the samples due to the corrosion attack.

Regarding the ground thin wall samples, R_{CT} values are generally one order of magnitude higher compared to the thin wall samples in as-cast condition. The values increase during immersion time for all the samples (Figure 17a). The values of R_{CT} for different samples, with regard to the position, and with different amounts of silicon, are close to each other. In the case of ground samples, values of R_{CP} represent the presence of the passive oxide layer. They remain almost constant for all of the samples, and show a similar trend.

In the case of ground thick plate (bulk) samples, reported in Figure 18, the behavior of 2.5 RGB and 4.5 RGB samples are very similar. After some initial fluctuation, values of R_{CT} remain almost constant for the two samples from 12 to 24 h of immersion, but never reach the high resistance showed by the ground thin wall samples. R_{CP} values increase from the first hour of immersion for sample 4.5 RGB.

SEM micrographs and map analysis of some selected corroded surfaces are shown in Figure 19. As clearly visible in Figure 19, corrosion is mainly localized in all the samples, and takes place especially in the eutectic region, at the interface between the silicon and aluminum and at the interface of aluminum grains and iron-rich intermetallic particles. These results are in accordance with results of other researchers about corrosion of Al–Si alloys in similar solutions [34,35].
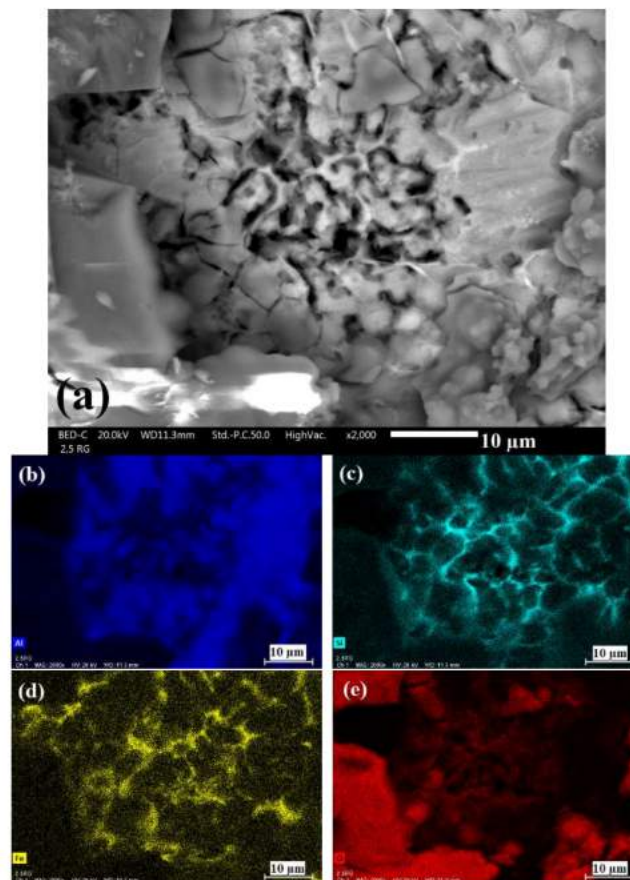
Figure 19. (**a**) SEM micrograph and elemental map analysis of corroded surface of sample 2.5 RG; (**b**) Al; (**c**) Si; (**d**) Fe; and (**e**) O.

4. Conclusions

In this paper, the corrosion behavior of the alloy in different parts of the component geometry were compared, and the microstructure macrosegregation due to Rheo-HPDC process was evaluated in terms of corrosion properties for two aluminum alloys containing 2.5 wt % and 4.5 wt % silicon. These alloys are prone to localized corrosion in the eutectic region at the interface between iron-rich intermetallic particles and the aluminum. Therefore, segregation of these phases influences the electrochemical behavior of the component. It was shown that the samples taken from different positions and different parts with various thicknesses differ in the amount of α_1-Al and α_2-Al particles. Samples also show a transverse macrosegregation. α_1-Al particles which are the solid fraction of the slurry, tend to segregate at the center of the samples, while the surface is richer in α_2-Al. Longitudinal segregation induces higher fraction of α_1-Al particles in the area nearer to the higher fraction of α_2-Al and the eutectic phase near the vent.

Both kinds of these segregations were shown to have influence on the corrosion behavior. A big change in the corrosion resistance was shown by grinding the samples. This is due to the as-cast surface morphology and composition, and to higher concentrations of intermetallic particles on the surface. In as-cast surface conditions, samples with higher amounts of α_2-Al and finer microstructure (near the vent) show slightly higher corrosion resistance.

Differently to most of the previous papers, the as-cast surface was tested. It was shown how the surface segregation and the increase of intermetallic particles on the very surface influence the pitting resistance of the component. Both ground thin wall and thick plate samples possess better corrosion resistance compared to the thin wall samples in as-cast condition. This improvement is due to the better surface condition. Nevertheless, relatively thinner samples show a higher corrosion resistance compared to the thicker samples. Surfaces of the rheocast component present a purely liquid microstructure due to the segregation, which makes them more resistant to corrosion when ground and therefore without surface defects.

Author Contributions: Maryam Eslami and Caterina Zanella conceived and designed the experiments; Maryam Eslami performed the experiments; Maryam Eslami, Mostafa Payandeh, Flavio Deflorian, Anders E. W. Jarfors and Caterina Zanella analyzed the data; Flavio Deflorian contributed reagents/materials/ analysis tools; Maryam Eslami, Mostafa Payandeh and Caterina Zanella wrote the paper.

Conflicts of Interest: The authors declare no conflict of interest.

References

1. Bonollo, F.; Gramegna, N.; Timelli, G. High-pressure die-casting: Contradictions and challenges. *JOM* **2015**, *67*, 901–908. [CrossRef]
2. Qi, M.; Kang, Y.; Zhou, B.; Liao, W.; Zhu, G.; Li, Y.; Li, W. A forced convection stirring process for Rheo-HPDC aluminum and magnesium alloys. *J. Mater. Process. Technol.* **2016**, *234*, 353–367. [CrossRef]
3. Ji, S.; Zhen, Z.; Fan, Z. Effects of rheo-die casting process on the microstructure and mechanical properties of AM50 magnesium alloy. *J. Mater. Sci. Technol.* **2005**, *21*, 1019–1024. [CrossRef]
4. Ji, S.; Wang, Y.; Watson, D.; Fan, Z. Microstructural evolution and solidification behavior of Al-Mg-Si alloy in high-pressure die casting. *Metall. Mater. Trans. A* **2013**, *44*, 3185–3197. [CrossRef]
5. Jin, C.K.; Jang, C.H.; Kang, C.G. Die design method for thin plates by indirect rheo-casting process and effect of die cavity friction and punch speed on microstructures and mechanical properties. *J. Mater. Process. Technol.* **2015**, *224*, 156–168. [CrossRef]
6. Fan, Z.; Ji, S.; Liu, G. Development of the rheo-diecasting process for Mg-alloys. *Mater. Sci. Forum* **2005**, *488–489*, 405–412. [CrossRef]
7. Moller, H.; Stumpf, W.E.; Pistorius, P.C. Influence of elevated Fe, Ni and Cr levels on tensile properties of SSM-HPDC Al-Si-Mg alloy F357. *Trans. Nonferr. Metals Soc. China* **2010**, *20*, s842–s846. [CrossRef]

8.   Flemings, M.C.; Riek, R.G.; Young, K.P. Rheocasting. *Mater. Sci. Eng.* **1976**, *25*, 103–117. [CrossRef]

9.   Fan, Z. Semisolid metal processing. *Int. Mater. Rev.* **2002**, *47*, 49–85. [CrossRef]

10. Atkinson, H.V. Alloys for semi-solid processing. *Solid State Phenom.* **2013**, *192–193*, 16–27. [CrossRef]

11. Payandeh, M. Rheocasting of Aluminium Alloys: Slurry Formation, Microstructure, and Properties. Ph.D. Thesis, Jönköping University, Jönköping, Sweden, April 2015.

12. Chen, Z.W. Skin solidification during high pressure die casting of Al–11Si–2Cu–1Fe alloy. *Mater. Sci. Eng. A* **2003**, *348*, 145–153. [CrossRef]

13. Laukli, H.I.; Gourlay, C.M.; Dahle, A.K. Migration of crystals during the filling of semi-solid castings. *Metall. Mater. Trans. A* **2005**, *36*, 805–818. [CrossRef]

14. Kaufmann, H.; Fragner, W.; Galovsky, U.; Uggowitzer, P.J. Fluctuations of Alloy Composition and Their Influence on Sponge Effect and Fluidity of A356-NRC. In *Proceedings of the 2nd International Light Metals Technology ConferenceProceedings of the 2nd International Light Metals Technology Conference, St. Wolfgang, Austria, 8–10 June 2005*; Kaufmann, H., Ed.; LKR-Verlag: St. Wolfgang, Austria, 2005.

15. Zabler, S.; Ershov, A.; Rack, A.; Garcia-Moreno, F.; Baumbach, T.; Banhart, J. Particle and liquid motion in semi-solid aluminium alloys: A quantitative in situ microradioscopy study. *Acta Mater.* **2013**, *61*, 1244–1253. [CrossRef]

16. Park, C.; Kim, S.; Kwon, Y.; Lee, Y.; Lee, J. Effect of microstructure on tensile behavior of thixoformed 357-T5 semisolid Al alloy. *Metall. Mater. Trans. A* **2004**, *35*, 1407–1410. [CrossRef]

17. Möller, H.; Masuku, E.P. The influence of liquid surface segregation on the pitting corrosion behavior of semi-solid metal high pressure die cast alloy F357. *TOCORRJ* **2009**, *2*, 216–220. [CrossRef]

18. Masuku, E.P.; Moller, H.; Curle, U.A.; Pistorius, P.C.; Li, W. Influence of surface liquid segregation on corrosion behavior of semi-solid metal high pressure die cast aluminium alloys. *Trans. Nonferr. Metals Soc. China* **2010**, *20*, s837–s841. [CrossRef]

19. Möller, H.; Curle, U.A.; Masuku, E.P. Characterization of surface liquid segregation in SSM-HPDC aluminium alloys 7075, 2024, 6082 and A201. *Trans. Nonferr. Metals Soc. China* **2010**, *20*, s847–s851. [CrossRef]

20. Guillaumin, V.; Mankowski, G. Localized corrosion of 6056 T6 aluminium alloy in chloride media. *Corros. Sci.* **2000**, *42*, 105–125. [CrossRef]

21. Eckermann, F.; Suter, T.; Uggowitzer, P.J.; Afseth, A.; Schmutz, P. The influence of MgSi particle reactivity and dissolution processes on corrosion in Al–Mg–Si alloys. *Electrochim. Acta* **2008**, *54*, 844–855. [CrossRef]

22. Zeng, F.-L.; Wei, Z.-L.; Li, J.-F.; Li, C.-X.; Tan, X.; Zhang, Z.; Zheng, Z.-Q. Corrosion mechanism associated with Mg$_2$Si and Si particles in Al–Mg–Si alloys. *Trans. Nonferr. Metals Soc. China* **2011**, *21*, 2559–2567. [CrossRef]

23. Liang, W.J.; Rometsch, P.A.; Cao, L.F.; Birbilis, N. General aspects related to the corrosion of 6xxx series aluminium alloys: Exploring the influence of Mg/Si ratio and Cu. *Corros. Sci.* **2013**, *76*, 119–128. [CrossRef]

24. Li, H.; Zhao, P.; Wang, Z.; Mao, Q.; Fang, B.; Song, R.; Zheng, Z. The intergranular corrosion susceptibility of a heavily overaged Al-Mg-Si-Cu alloy. *Corros. Sci.* **2016**, *107*, 113–122. [CrossRef]

25. Brito, C.; Vida, T.; Freitas, E.; Cheung, N.; Spinelli, J.E.; Garcia, A. Cellular/dendritic arrays and intermetallic phases affecting corrosion and mechanical resistances of an Al–Mg–Si alloy. *J. Alloys Compd.* **2016**, *673*, 220–230. [CrossRef]

26. Li, C.; Sun, J.; Li, Z.; Gao, Z.; Liu, Y.; Yu, L.; Li, H. Microstructure and corrosion behavior of Al–10%Mg$_2$Si cast alloy after heat treatment. *Mater. Charact.* **2016**, *122*, 142–147. [CrossRef]

27. Kairy, S.K.; Rometsch, P.A.; Diao, K.; Nie, J.F.; Davies, C.H.J.; Birbilis, N. Exploring the electrochemistry of 6xxx series aluminium alloys as a function of Si to Mg ratio, Cu content, ageing conditions and microstructure. *Electrochim. Acta* **2016**, *190*, 92–103. [CrossRef]

28. Svenningsen, G.; Lein, J.E.; Bjørgum, A.; Nordlien, J.H.; Yu, Y.; Nisancioglu, K. Effect of low copper content and heat treatment on intergranular corrosion of model AlMgSi alloys. *Corros. Sci.* **2006**, *48*, 226–242. [CrossRef]

29. Rehim, S.S.A.; Hassan, H.H.; Amin, M.A. Chronoamperometric studies of pitting corrosion of Al and (Al–Si) alloys by halide ions in neutral sulphate solutions. *Corros. Sci.* **2004**, *46*, 1921–1938. [CrossRef]

30. Tahamtan, S.; Boostani, A.F. Evaluation of pitting corrosion of thixoformed A356 alloy using a simulation model. *Trans. Nonferr. Metals Soc. China* **2010**, *20*, 1602–1606. [CrossRef]

31. Park, C.; Kim, S.; Kwon, Y.; Lee, Y.; Lee, J. Mechanical and corrosion properties of rheocast and low-pressure cast A356-T6 alloy. *Mater. Sci. Eng. A* **2005**, *391*, 86–94. [CrossRef]

32. Bastidas, J.M.; Forn, A.; Baile, M.T.; Polo, J.L.; Torres, C.L. Pitting corrosion of A357 aluminium alloy obtained by semisolid processing. *Mater. Corros.* **2001**, *52*, 691–696. [CrossRef]

33. Pech-Canul, M.A.; Pech-Canul, M.I.; Bartolo-Pérez, P.; Echeverría, M. The role of silicon alloying addition on the pitting corrosion resistance of an Al-12 wt %Si alloy. *Electrochim. Acta* **2014**, *140*, 258–265. [CrossRef]

34. Arrabal, R.; Mingo, B.; Pardo, A.; Mohedano, M.; Matykina, E.; Rodríguez, I. Pitting corrosion of rheocast A356 aluminium alloy in 3.5 wt % NaCl solution. *Corros. Sci.* **2013**, *73*, 342–355. [CrossRef]

35. Tahamtan, S.; Boostani, A.F. Quantitative analysis of pitting corrosion behavior of thixoformed A356 alloy in chloride medium using electrochemical techniques. *Mater. Des.* **2009**, *30*, 2483–2489. [CrossRef]

36. Larsen, M.H.; Walmsley, J.C.; Lunder, O.; Mathiesen, R.H.; Nisancioglu, K. Intergranular corrosion of copper-containing AA6xxx AlMgSi aluminum alloys. *J. Electrochem. Soc.* **2008**, *155*, C550–C556. [CrossRef]

37. Zhan, H.; Mol, J.M.C.; Hannour, F.; Zhuang, L.; Terryn, H.; de Wit, J.H.W. The influence of copper content on intergranular corrosion of model AlMgSi(Cu) alloys. *Mater. Corros.* **2008**, *59*, 670–675. [CrossRef]

38. Svenningsen, G.; Larsen, M.H.; Walmsley, J.C.; Nordlien, J.H.; Nisancioglu, K. Effect of artificial aging on intergranular corrosion of extruded almgsi alloy with small Cu content. *Corros. Sci.* **2006**, *48*, 1528–1543. [CrossRef]

39. Qian, M.; Li, D.; Liu, S.B.; Gong, S.L. Corrosion performance of laser-remelted Al–Si coating on magnesium alloy AZ91D. *Corros. Sci.* **2010**, *52*, 3554–3560. [CrossRef]

40. Yu, Y.; Kim, S.; Lee, Y.; lee, J. Phenomenological observations on mechanical and corrosion properties of thixoformed 357 alloys: A comparison with permanent mold cast 357 alloys. *Metall. Mater. Trans. A* **2002**, *33*, 1399–1412. [CrossRef]

41. Eslami, M.; Fedel, M.; Speranza, G.; Deflorian, F.; Zanella, C. Deposition and characterization of cerium-based conversion coating on HPDC low Si content aluminum alloy. *J. Electrochem. Soc.* **2017**, *164*, C581–C590. [CrossRef]

42. Wessén, M.; Cao, H. The RSF Technology: A Possible Breakthrough for Semi-Solid Casting Processes. In Proceedings of the International Conference of High Tech Die Casting, Vicenza, Italy, 21–22 September 2006.

43. Cano, E.; Lafuente, D.; Bastidas, D.M. Use of EIS for the evaluation of the protective properties of coatings for metallic cultural heritage: A review. *J. Solid State Electrochem.* **2010**, *14*, 381–391. [CrossRef]

44. Letardi, P. 7—Electrochemical measurements in the conservation of metallic heritage artefacts: An overview. In *Corrosion and Conservation of Cultural Heritage Metallic Artefacts*; Watkinson, D., Angelini, E., Adriaens, A., Eds.; Woodhead Publishing: Cambridge, UK, 2013; pp. 126–148.

45. Kirkwood, D.H.; Suery, M.; Kapranos, P.; Atkinson, H.V.; Young, K.P. *Semi-Solid Processing of Alloys*; Springer: New York, NY, USA, 2010.

46. Belov, N.A.; Aksenov, A.A. *Iron in Aluminum Alloys: Impurity and Alloying Element*; Taylor & Francis Inc.: New York, NY, USA, 2002.

47. Sundman, B.; Jansson, B.; Andersson, J.-O. The thermo-calc databank system. *Calphad* **1985**, *9*, 153–190. [CrossRef]

48. Andersson, J.-O.; Helander, T.; Höglund, L.; Shi, P.; Sundman, B. Thermo-Calc & DICTRA, computational tools for materials science. *Calphad* **2002**, *26*, 273–312.

49. Payandeh, M.; Jarfors, A.E.W.; Wessén, M. Solidification sequence and evolution of microstructure during rheocasting of four Al-Si-Mg-Fe alloys with low Si content. *Metall. Mater. Trans. A* **2016**, *47*, 1215–1228. [CrossRef]

50. Easton, M.; Kaufmann, H.; Fragner, W. The effect of chemical grain refinement and low superheat pouring on the structure of NRC castings of aluminium alloy Al–7Si–0.4 Mg. *Mater. Sci. Eng. A* **2006**, *420*, 135–143. [CrossRef]

51. Zhu, B.; Seifeddine, S.; Persson, P.O.Å.; Jarfors, A.E.W.; Leisner, P.; Zanella, C. A study of formation and growth of the anodised surface layer on cast Al-Si alloys based on different analytical techniques. *Mater. Des.* **2016**, *101*, 254–262. [CrossRef]

52. Gourlay, C.; Dahle, A.; Nagira, T.; Nakatsuka, N.; Nogita, K.; Uesugi, K. Granular deformation mechanisms in semi-solid alloys. *Acta Mater.* **2011**, *59*, 4933–4943. [CrossRef]

53. Payandeh, M.; Jarfors, A.E.W.; Wessén, M. Influence of microstructural inhomogeneity on fracture behaviour in SSM-HPDC Al-Si-Cu-Fe component with low Si content. *Solid State Phenom.* **2015**, *217–218*, 67–74. [CrossRef]

54. Govender, G.; Möller, H. Evaluation of surface chemical segregation of semi-solid cast aluminium alloy A356. *Solid State Phenom.* **2008**, *141–143*, 433–438. [CrossRef]

55. Dinnis, C.M.; Dahle, A.K.; Taylor, J.A. Three-dimensional analysis of eutectic grains in hypoeutectic Al–Si alloys. *Mater. Sci. Eng. A* **2005**, *392*, 440–448. [CrossRef]

56. Mingo, B.; Arrabal, R.; Pardo, A.; Matykina, E.; Skeldon, P. 3D study of intermetallics and their effect on the corrosion morphology of rheocast aluminium alloy. *Mater. Charact.* **2016**, *112*, 122–128. [CrossRef]

57. Ji, S.; Das, A.; Fan, Z. Solidification behavior of the remnant liquid in the sheared semisolid slurry of Sn–15 wt % Pb alloy. *Scripta Mater.* **2002**, *46*, 205–210. [CrossRef]

58. Wang, X.-H.; Wang, J.-H.; Fu, C.-W. Characterization of pitting corrosion of 7A60 aluminum alloy by EN and EIS techniques. *Trans. Nonferr. Metals Soc. China* **2014**, *24*, 3907–3916. [CrossRef]

59. Amin, M.A. Uniform and pitting corrosion events induced by SCN^- anions on Al alloys surfaces and the effect of UV light. *Electrochim. Acta* **2011**, *56*, 2518–2531. [CrossRef]

60. Amin, M.A.; Hassan, H.H.; Hazzazi, O.A.; Qhatani, M.M. Role of alloyed silicon and some inorganic inhibitors in the inhibition of meta-stable and stable pitting of Al in perchlorate solutions. *J. Appl. Electrochem.* **2008**, *38*, 1589–1598. [CrossRef]

61. Despić, A.; Parkhutik, V.P. Electrochemistry of aluminum in aqueous solutions and physics of its anodic oxide. In *Modern Aspects of Electrochemistry No. 20*; Bockris, J.O.M., White, R.E., Conway, B.E., Eds.; Springer: Boston, MA, USA, 1989; pp. 401–503.

62. Moreto, J.A.; Marino, C.E.B.; Filho, W.W.B.; Rocha, L.A.; Fernandes, J.C.S. SVET, SKP and EIS study of the corrosion behaviour of high strength Al and Al–Li alloys used in aircraft fabrication. *Corros. Sci.* **2014**, *84*, 30–41. [CrossRef]